EARLY CAREER SCHOLARS IN MATERIALS SCIENCE

Effect of scanning strategy on microstructure and mechanical properties of a biocompatible Ti–35Nb–7Zr–5Ta alloy processed by laser-powder bed fusion

Weverson Capute Batalha[1,2], Rodolfo Lisboa Batalha[3,a)] (ORCID), Konrad Kosiba[4],
Claudio Shyinti Kiminami[5], Piter Gargarella[1,5,6]

[1] Graduate Program in Materials Science and Engineering, Federal University of São Carlos, Rod. Washington Luiz, km 235,
São Carlos CEP: 13.565-905, Brazil
[2] LEPMI, Grenoble INP, Grenoble Alpes University, 38402 Saint Martin d'Hères, France
[3] Materials and Technologies, Department of Research, Development and Innovation, Instituto de Soldadura e Qualidade, Avenida Professor
Dr. Cavaco Silva, 33 Taguspark, 2740-120 Porto Salvo, Oeiras, Portugal
[4] Leibniz-IFW Dresden, Institute for Complex Materials, Helmholtzstraße 20, 01069 Dresden, Germany
[5] Department of Materials Engineering, Federal University of São Carlos, Rod. Washington Luiz, km 235, São Carlos CEP: 13.565-905, Brazil
[6] Center for Characterization and Development of Materials (CCDM), Federal University of São Carlos, Rod. Washington Luiz, km 235,
São Carlos CEP: 13.565-905, Brazil
a) Address all correspondence to this author. e-mail: rlbatalha@isq.pt

The influence of scanning strategy (SS) on microstructure and mechanical properties of a Ti–35Nb–7Zr–5Ta alloy processed by laser-powder bed fusion (L-PBF) is investigated for the first time. Three SSs are considered: unidirectional-Y; bi-directional with 79° rotation (R79); and chessboard (CHB). The SSs affect the type and distribution of pores. The highest relative densities and more homogeneous distribution of pores are obtained with R79 and CHB scanning strategies, whereas aligned pores are formed in the unidirectional-Y. The SSs show direct influence on the crystallographic texture with unidirectional-Y strategy showing fiber texture. The R79 strategy results in a weak texture and the CHB scanning strategy forms a randomly oriented heterogeneous grain structure. The lowest Young modulus is obtained with the unidirectional-Y strategy, whereas the R79 strategy results in the highest yield strength. It is shown that the SSs may be used for tuning the microstructure of a beta-Ti alloy in L-PBF.

Rodolfo Lisboa Batalha

Rodolfo Lisboa Batalha Dr. Rodolfo Batalha is a researcher on additive manufacturing at the Instituto de Soldadura e Qualidade in Portugal, currently responsible for PBF-LB and post-processing labs. His research interests are materials development for additive manufacturing, materials characterization, microstructure, mechanical properties, and design for additive manufacturing. He earned his Bachelor of Science degree in Metallurgical Engineering from Brazil's Universidade Federal de Ouro Preto in 2012, and his MS in Materials Engineering from the same university in 2015. In 2019, he was awarded his Ph.D. in Materials Science and Engineering by the Universidade Federal de Sao Carlos, also in Brazil. Dr. Batalha has experience in the development of new alloys for additive manufacturing, evaluation of metallic powders, and parameters' optimization for the laser-powder bed fusion process, with an emphasis on the design of microstructure. He has also worked with (micro)structural characterization, mechanical tests, and analysis by micro X-ray computed tomography of metallic materials. He has worked in the steel industry conducting innovation projects and process improvement projects.

Introduction

Additive manufacturing (AM) is an emerging technology receiving great attention in recent years. It allows the fabrication of near-net-shaped parts with less material and energy waste than conventional processes [1]. In general, metallic feedstock such as metallic powder or wire is subjected to repetitive melting-solidification cycles characterized by high heating and cooling rates. Moreover, the previously deposited layers are remelted by the energy source or heat-treated by a directional heat flow from the melt pool toward the substrate [2].

The suitability of metal AM to fabricate individualized parts has led to various studies reporting metal AM as a promising route for the production of orthopedic implants [3]. Investigations and development of novel metallic biomaterials have remained a topic of high interest in academia and industry aiming for the fabrication of individualized implants that could last for the entire patient's life. Examples of metallic materials used for implants include cobalt-chromium (Co–Cr) alloys, 316L stainless steel, commercial pure titanium (CP-Ti), and Ti–6Al–4V alloy. The problem with those materials is the toxicity of some elements like Ni, Co, Al, V, and Cr. In addition, they present a higher elastic modulus than the bone causing bone reabsorption problems and loss of the prostheses within a few years [4].

Ti alloys exhibit good corrosion resistance, mechanical properties, and biocompatibility. In addition, they show a lower Young's modulus compared to 316L and Co–Cr alloys. Nonetheless, the widely used Ti–6Al–4V alloy and CP-Ti still show significantly higher Young's modulus than the compact bone. Therefore, new compositions of biocompatible beta-TiNb alloys have been considered to replace the more established Ni–Ti and Ti–6Al–4V alloys used in implants because of their lower Young's modulus and excellent biocompatibility [4, 5]. Furthermore, the addition of non-toxic elements such as Zr, Nb, and Ta to beta-TiNb alloys has shown to be responsible for reducing Young's modulus. These elements have been used in several new beta-Ti alloys as Ti–18Zr–14Nb [6], Ti–29Nb–13Ta–4.6Zr [7], Ti–24Nb–4Zr–8Sn [8], and Ti–35Nb–7Zr–5Ta (TNZT) [9].

Laser-powder bed fusion (L-PBF), also known as selective laser melting (SLM), is one of the most widely used metal AM techniques to fabricate metallic implants [10]. The process consists of fully melting a metallic powder in a layer-by-layer manner by scanning a highly focused laser beam onto the powder bed. As a result, fully dense parts can be realized. During the process, the chamber is filled with inert gas (Ar or N_2) to protect the powder against oxidation [10, 11]. The most influential processing parameters that directly affect the characteristics of the final component are laser power, scanning speed, layer thickness, and hatching distance. Parameters such as the laser wavelength and powder particle size distribution (PSD) are normally fixed. The scanning parameters define the volumetric energy input which is optimized according to the specific material and envisaged geometry [10–12]. The resulting microstructure is directly dependent on the melt pool shape and size. The L-PBF process has generally smaller melt pools than laser welding and presents the highest cooling rate among the metal AM processes, due to the rapid scanning speeds [10–13]. Therefore, the processing parameters can be varied to result in a part with different densification and surface roughness [5], and parameter optimization is vital to avoid the formation of defects such as lack-of-fusion, keyholes, and balling [13].

The scanning strategy defined by the length and pattern of the scanning vectors of the laser is another important parameter that should be optimized. It can be unidirectional or bidirectional and undergo rotation between subsequent layers or even within the same layer [5]. With other parameters fixed, the scanning strategy has a significant influence on the quality of the final part. Applying computational simulation and experiments, Song et al. [14] showed that the scanning strategy affects the temperature field and residual stress distribution. However, the authors did not find the scanning strategy to have a great influence on the melt pool size.

Valente et al. [15] studied a Ti–6Al–4V alloy showing that the scanning strategy influences the type and volume of porosity, resulting in lack-of-fusion in some cases. It was also shown that it impacts the microstructure refinement and phase formation. With a line scanning strategy, the grains of the β-phase remained in the aligned in the printing direction, due to the lack of rotation between adjacent layers. In the island scanning strategy, the β-grains appeared irregular and the martensite morphology was non-homogeneous.

Han et al. [16] also investigated the effects of scanning strategy in the Ti–6Al–4V alloy. The authors developed a scanning strategy with rotation from outside to inside aiming to reduce the surface roughness and provide more uniformity to the parts. For the Ti-5553 alloy, Schwab et al. [17] studied the influence of using a chessboard scanning strategy compared to a stripe strategy with 45° rotation between adjacent layers. The authors highlighted the importance of properly selecting an adequate hatching distance between the islands of the chessboard strategy. The results showed a direct impact on the porosity distribution of the samples.

Although some works have reported effects of scanning strategy on the quality of parts manufactured by L-PBF, there are limited studies on the design of microstructure of beta-Ti alloys through scanning strategies. In addition, to the best of our knowledge, there are no reported studies on the effects of the scanning strategy for the biocompatible β-Ti–35Nb–7Zr–5Ta alloy. Therefore, this work aims to investigate how varying the scanning strategies affect the microstructure, densification, and mechanical properties of the TNZT alloy synthesized by L-PBF.

Results and discussion

Chemical analysis and powder characterization

Table 1 shows the chemical composition of the TNZT powder and the as-built samples produced by L-PBF with different scanning strategies.

It is noticed that the chemical composition of the samples is close to the nominal composition. The bulk samples showed higher oxygen than the powder which suggests that during the melting the melt pool is enriched in oxygen. This is related to the alloy's high affinity to oxygen [18].

The spherical morphology of the TNZT powder particles is shown in Fig. 1(a) and (b). The powder particles present a smooth surface, and only a slight presence of satellites is observed.

The microstructure of the powder is shown in Fig. 1(c). The powder presents an equiaxed-dendritic solidification structure related to a high cooling rate in the gas atomization process of the TNZT alloy. In addition, the EDS maps [Fig. 1(d)–(g)] show a homogeneous chemical distribution of the elements in the powder particles.

Effect of the scanning strategies on relative density

Table 2 presents the densities of the samples fabricated by L-PBF with unidirectional-Y, R79, and CHB scanning strategies. The results were compared with a theoretically fully dense as-cast sample to calculate the relative density. The three scanning strategies resulted in samples with a relative density exceeding 99.0%. The pore distribution and shape were further investigated with μ-XCT (Fig. 2).

It is seen that the pores tend to align in the direction of the scanning vector within the layer when the unidirectional-Y scanning strategy was employed [Fig. 2(a)]. By rotating the vectors with R79 [Fig. 2(b)] and CHB [Fig. 2(c)] strategies, a more

TABLE 1: Chemical composition and oxygen contents of the Ti-35Nb-7Zr-5Ta powder and L-PBF samples.

Sample	Ti	Nb	Zr	Ta	O
TNZT powder	Bal	34.0±1.5	6.60±0.10	4.10±0.02	0.050±0.002
Unidirectional-Y	Bal	37.7±0.1	6.50±0.04	5.20±0.10	0.124±0.007
R79	Bal	37.6±0.1	6.49±0.04	5.20±0.10	0.126±0.001
CHB	Bal	36.9±0.1	6.39±0.04	5.40±0.10	0.131±0.001

TABLE 2: Relative density of as-built samples of the TNZT alloy produced by L-PBF with three different scanning strategies.

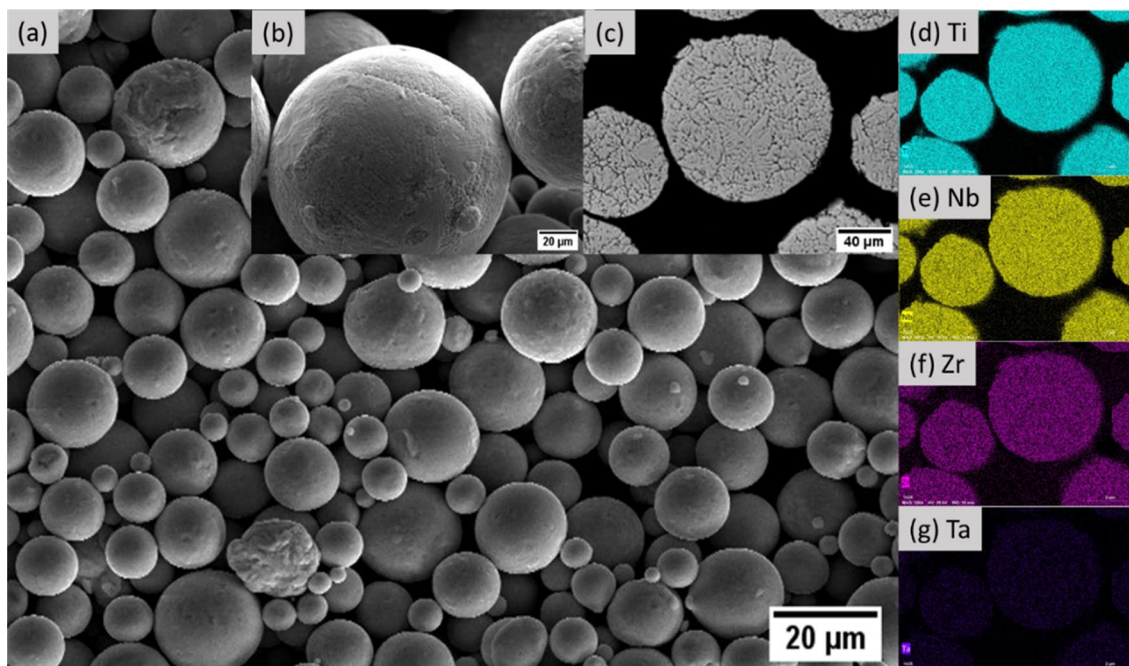| Sample	Density (g/cm³)	Relative density by Archimedes (%)
Unidirectional-Y	5.72±0.01	99.5
R79	5.75±0.01	100
CHB	5.77±0.04	100

Figure 1: TNZT powder: (a, b) powder particles morphology, (c) dendritic microstructure, and d-g) EDS analysis of the powder particles. The maps in (d–g) correspond to Ti, Nb, Zr, and Ta, respectively.
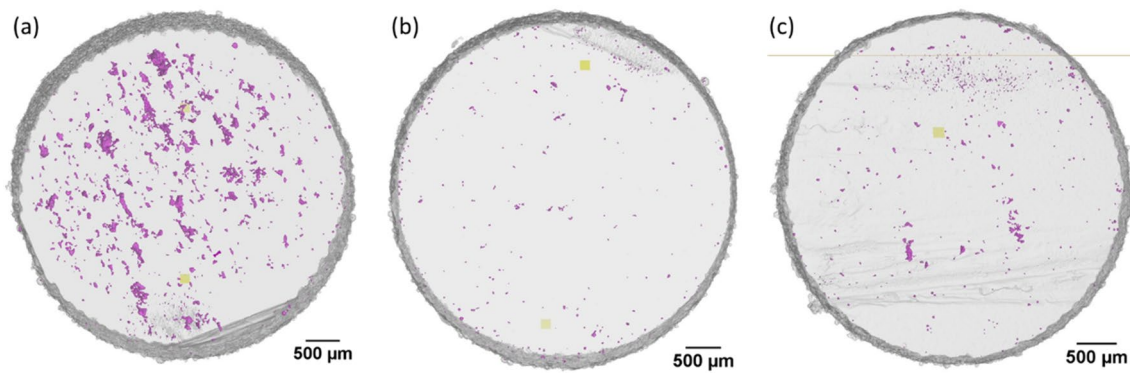
Figure 2: The μ-XCT images with projected pores on the cross-section plane: (a) unidirectional-Y, (b) R79, and (c) CHB scanning strategies. The purple color indicates defects.

homogeneous distribution of pores is observed. Furthermore, the pores are more circular in the samples produced with the R79 and CHB strategies than in the sample with the unidirectional-Y. The CHB scanning strategy showed in Fig. 2(c) resulted in pores mostly concentrated in regions that coincide with the boundaries of the islands.

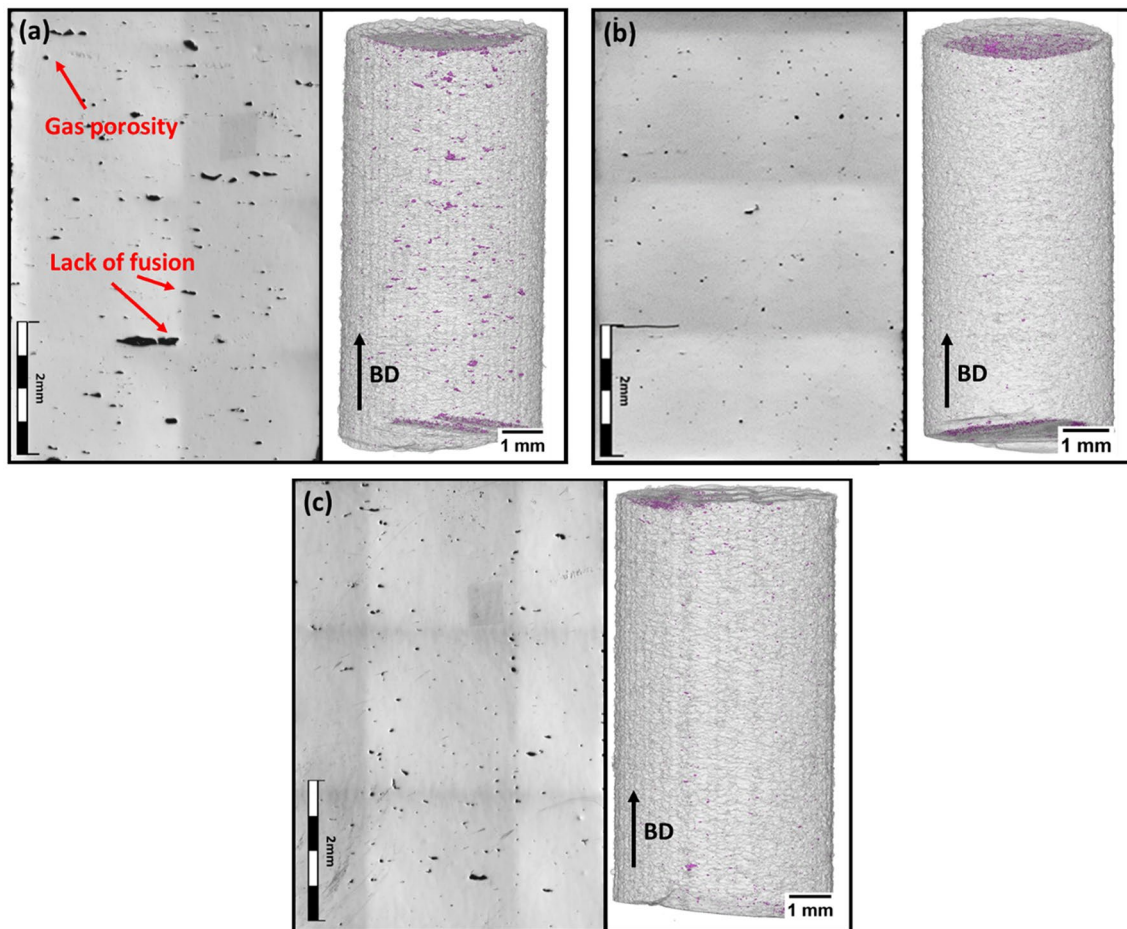Figure 3 shows images obtained by confocal optical microscope and μ-XCT along the building direction of the samples

Figure 3: Confocal (left) and μ-XCT (right) images of the as-built samples produced by L-PBF with different scanning strategies: (a) unidirectional-Y, (b) R79, and (c) CHB.

produced with the unidirectional-Y, R79, and CHB scanning strategies.

At least two types of defects are detected: (i) Gas porosity with a spherical shape resulting from the shielding gas or entrapped gas into the powder particles, and (ii) Lack-of-fusion that typically occurs due to an insufficient melt pool penetration in previous layers. The latter pores are larger and show sharp edges, which can act as stress concentrators under loading [10].

The unidirectional-Y scanning strategy resulted in lack-of-fusion [Fig. 3(a)], which explains its lowest density among all samples produced (Table 1). The R79 scanning strategy results in a more uniform distribution of mainly circular pores [Fig. 3(b)], while the CHB scanning strategy showed pore accumulation between the islands [Fig. 3(c)], similarly to previous works about Ti- and Cu-based alloys [17, 19]. However, this was not a definitive pattern as some randomly distributed pores are also observed in the CHB strategy, which is related to the 90° rotation between islands in the CHB scanning strategy.

Microstructure of the L-PBF as-built samples

The phase constitution of the as-built samples produced by L-PBF with different scanning strategies was analyzed by XRD (please see Figure S1 in Supplementary Material). The bulk samples produced by unidirectional-Y, R79, and CHB scanning strategies show a β single-phase structure. The high concentration of β stabilizing elements in the TNZT alloy combined with the high cooling rates of the L-PBF process is sufficient to inhibit the precipitation of other phases [20]. Therefore, although the scanning strategy is expected to influence the heat distribution between adjacent layers, it does not affect the phase formation of the TNZT alloy. Moreover, a reflection separation at 56° and 70° was detected. Kheradmandfard et al. [21] observed this double reflection in a β-Ti-29Nb-13Ta-4.6Zr alloy and suggested that it is related to a spinodal decomposition of the β phase into β1 and β2 phases, with the difference being the lattice parameters of each of the β phases. This phase separation was also observed in the work of Afonso et al. [22] in an as-cast and age-hardened TNZT alloy.

Table 3 shows the dimensions of the melt pool for the different strategies studied. The melt pools of the fabricated parts were observed by optical microscopy in the building direction. The measurement of the melt pool dimensions was performed using the ImageJ software.

Melt pool geometry will affect the local solidification rate and consequently the microstructure. It is dependent on material thermophysical properties and processing parameters, such as laser power and scanning speed. In a previous work, Song et al. [14] showed that there was no significant influence of the scanning strategy on the melt pool dimensions for L-PBF-fabricated Ti6Al4V. Those results corroborate with the unidirectional-Y and CHB strategies studied in the present work. However, the dimensions of the melt pool in samples with the R79 scanning strategy show a significant difference in the melt pool depth. At the unidirectional-Y and CHB with 90° rotation scanning strategies, the laser remelts the same region of adjacent layers. The remelting of a solidified previous layer occurs with higher laser reflection than if it was a layer of powder bed, resulting in shallow melt pools. The effect of remelting has already been reported to be responsible for decreasing melt pool depth and changing melt pool shape [23]. On the other hand, samples with the R79 scanning strategy showed the greatest values for the melt pool depth. For the R79° strategy, the laser will only melt the same region again after many layers. Therefore, the laser will be mainly melting the powder bed and not a solid substrate, resulting in a higher energy absorption and, hence, a melt pool with higher depth. The melt pool dimensions in the samples produced with unidirectional-Y and CHB are similar.

Figure 4 shows the solidification structure along the building direction of samples produced by L-PBF with the different scanning strategies.

The formation of a cellular structure independently of the scanning strategy with a high degree of cell refinement is visible in samples produced with the three scanning strategies (cell thickness of approximately 600 nm). Several studies also showed the formation of similar microstructures for β-Ti alloys [20, 24–27].

Figure 4(a) and (b) present the microstructure of the sample produced using the R79 scanning strategy. The micrographs show microsegregation in the melt pool boundaries and a similar feature is observed in the sample produced with the unidirectional-Y and CHB scanning strategies [Fig. 4(c, d) and (e, f)]. In addition, columnar grains are observed, formed by the alignment of cellular crystals inside the melt pool. Grain growth perpendicular to the melt pool boundary is also observed and the competitive growth mechanism is indicated by the direction of the cellular growth, where the cells aligned along the direction of maximum heat extraction are favored.

The cellular solidification structure of the as-built TNZT samples results from the high thermal gradient and the high cooling rates of the L-PBF process, which directly influence the grain refinement of the microstructure. The ⟨001⟩ direction is

TABLE 3: Melt pool dimensions for the TNZT alloy produced by L-PBF with the different scanning strategies.

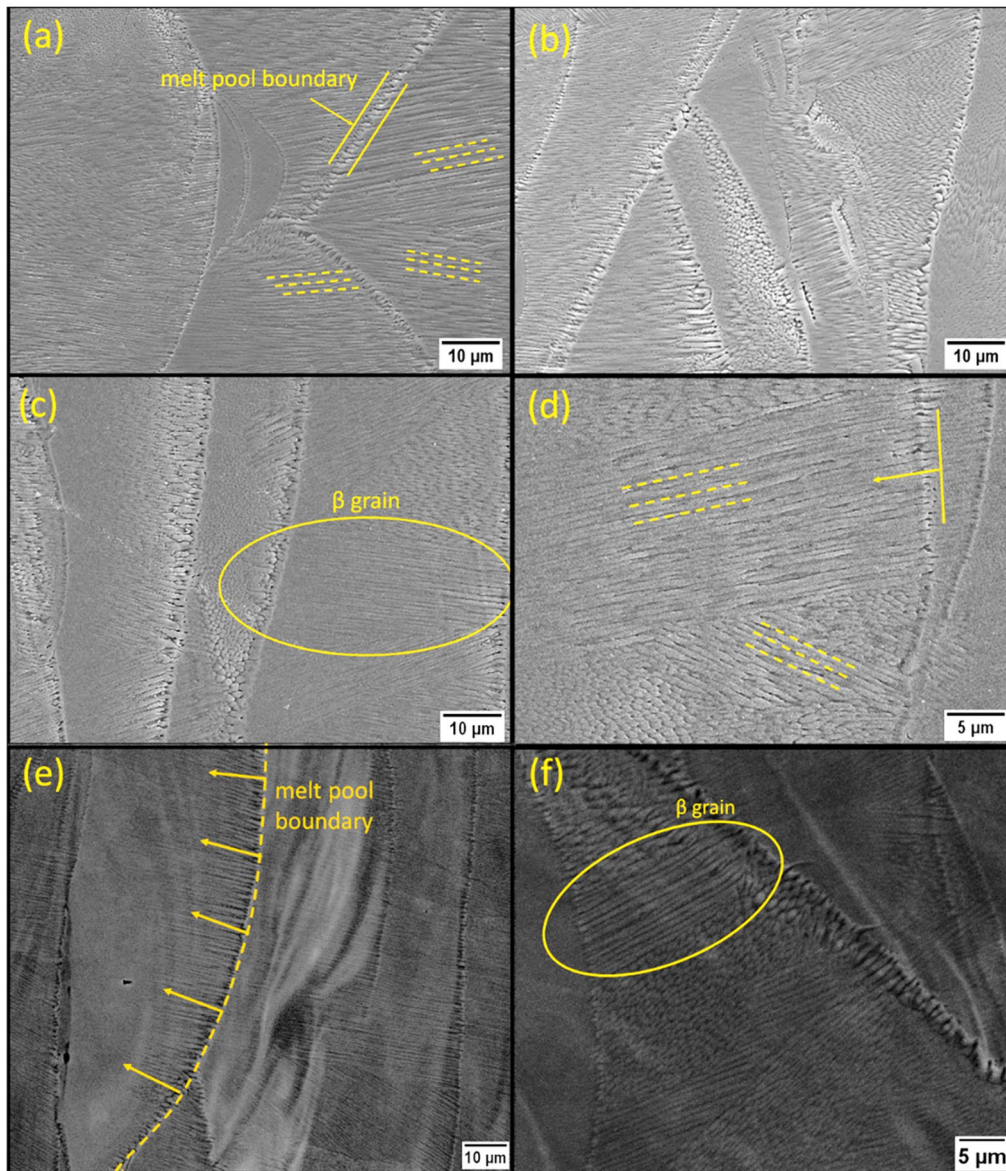| Sample	Width (μm)	Depth (μm)
Unidirectional-Y	192.5 ± 21.6	58.1 ± 9.8
R79	189.7 ± 73.2	93.9 ± 29.4
CHB	200.6 ± 29.7	58.2 ± 8.6

Figure 4: SEM micrographs of samples of the TNZT alloy produced by L-PBF with three different scanning strategies: (a, b) R79, (c, d) unidirectional-Y, and (e, f) CHB.

the easy-growth direction and the remelting of previous tracks induced by the unidirectional-Y and the CHB scanning strategies also influence the grain structure of the samples [25].

Figure 5 shows the EBSD results for the three scanning strategies. It is seen that the differences obtained in the crystallographic textures as a result of the different scanning strategies are associated with the differences in the melt pool shape. The shape will influence the curvature and morphology of the resulting grains and the direction in which the cells tend to grow due to the direction of heat extraction [28, 29]. In addition, the local temperature field in the interface where growth occurs depends on the scanning strategy and will impact the

grain growth direction. The columnar grains are growing along the build direction, with cellular crystals perpendicular to the melt pool boundary, and ultimately forming elongated grains (longer than the melt pool depth) seen in the SEM images and the EBSD maps (Figs. 4 and 5, respectively).

The epitaxial grain growth is evidenced by the presence of predominantly columnar grains growing throw several layer thicknesses (40 μm) in samples produced with R79 [Fig. 5(a)] and unidirectional-Y [Fig. 6(c)] scanning strategies. The CHB scanning strategy [Fig. 5(b)] resulted in a more heterogeneous grain morphology with equiaxed grains forming in the contours of the islands with columnar grains in the center of the islands.
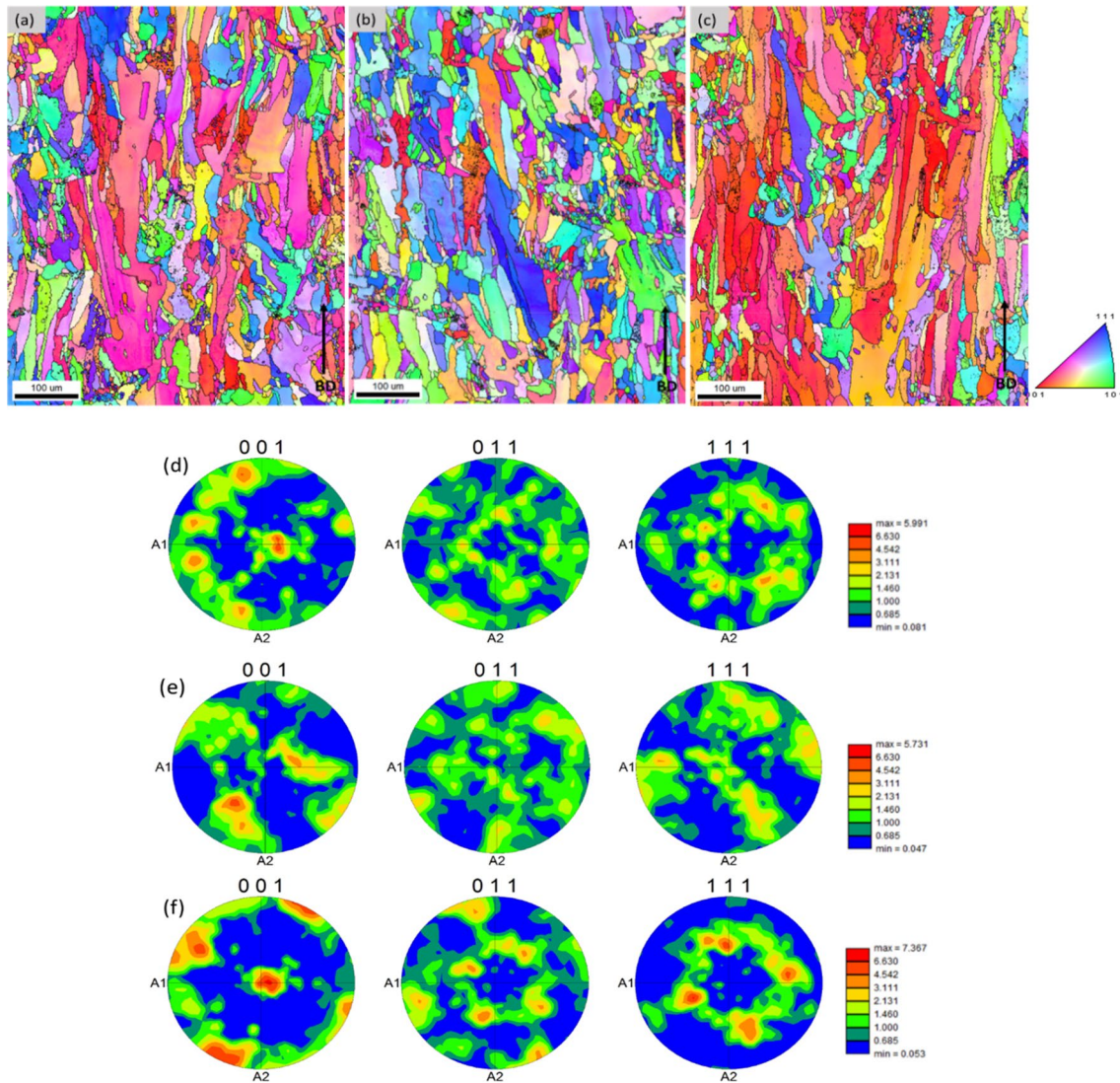
Figure 5: EBSD maps: Inverse pole figures in the z-axis (IPF-z) of as-built cylinders of the TNZT microstructure produced by L-PBF with (a) R79, (b) CHB and (c) unidirectional-Y scanning strategies, and the corresponding pole figures on {001}, {011}, and {111} stereographic planes in (d), (e) and (f), respectively.
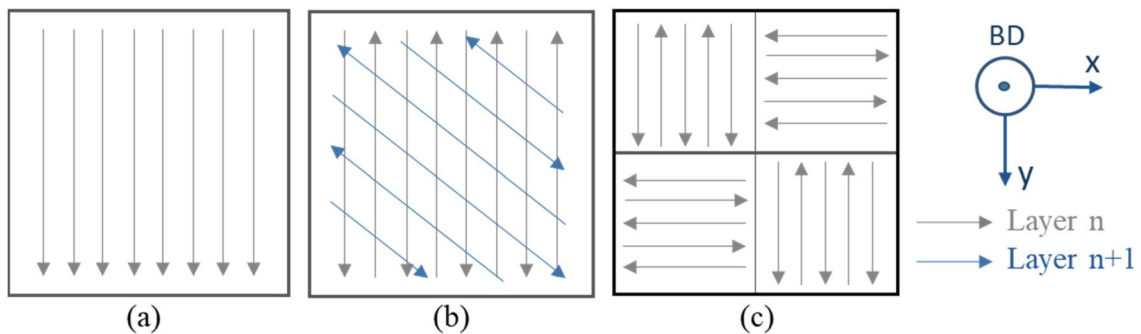

Figure 6: The three laser scanning strategies used are: (a) unidirectional in the *y*-axis without rotation (unidirectional-Y), (b) bidirectional with 79° rotation (R79), and (c) chessboard (CHB) bidirectional with 90° rotation between islands with 1.5×1.5 mm^2.

The sample produced with the R79 strategy [Fig. 5(a)] presented a weak tendency of grain alignment along the ⟨001⟩ direction. The aspect ratio (w/L, where 1 is an equiaxial grain) of the grains is in the range of 0.15–0.30 which confirms the columnar morphology. The respective pole figure [Fig. 5(d)] shows more intense poles in the {001} stereographic plane along the axis of the building direction, while in the {111} pole figure the formation of a more intense ring is noted. Therefore, for the samples produced with the R79 scanning strategy, a weak ⟨001⟩ texture is observed. In the R79 scanning strategy, the laser path varies at a certain angle to the previous layer, and the direction of the higher thermal gradient changes, altering the texture domain. New grains grow then in a slightly different direction than the previously solidified grains resulting in greater randomness in grain orientation.

The sample produced with the CHB scanning strategy [Fig. 5(b) and (e)] shows rather randomly oriented grains. In the sample produced using the CHB strategy, the orientations seem to constantly change along the growing direction within the melt pool. In addition, laser remelting occurs in the boundaries of overlapping islands. This results in smaller and randomly oriented grains (absence of crystallographic texture). The grain morphology is still predominantly columnar, with an aspect ratio between 0.20 and 0.40, although with equiaxial grains formed in the boundaries of overlapping islands.

Among the three scanning strategies, the unidirectional-Y showed the strongest texture [Fig. 5(c) and (f)]. The respective EBSD map [Fig. 5(c)] shows a stronger alignment of grains along the ⟨001⟩ direction. The pole figures [Fig. 5(f)] represent the development of a fiber texture. The grains also have a columnar morphology with an even lower aspect ratio in the range of 0.10–0.30. The laser beam scans the powder bed in the same direction during L-PBF processing with the unidirectional-Y strategy. Therefore, the grains continue to grow along the direction of maximum heat extraction resulting in elongated grains readily reflected in stronger texture. Wei et al. [30] showed this difference in grain orientation by numerical modeling of heat transfer combined with experiments to understand the texture formation in a nickel-based alloy. The authors compared the unidirectional and bidirectional scanning strategies. The difference in heat distribution in the bidirectional scanning strategy in comparison to the unidirectional scanning strategy affects the growth pattern of the dendrites. In the latter, there is a deviation between the dendrite grain growth and the direction of maximum heat flow.

Mechanical properties

Table 4 and Fig. S2 (please refer to Supplementary Material) present the results of the compression tests of the TNZT alloy produced by L-PBF with the three scanning strategies. As a first result, it was observed that all samples showed excellent ductility

TABLE 4: Summary of compression properties of the TNZT alloy produced by L-PBF with different scanning strategies.

Sample	E (GPa)	$\sigma_{0.2\%}$ (MPa)
Unidirectional-Y (this work)	47 ± 11	452 ± 30
R79 (this work)	49 ± 8	466 ± 16
CHB (this work)	50 ± 8	436 ± 33
TNZT as-cast [31]	48 ± 4	469 ± 42
TNZT as-built [31]	45 ± 5	430 ± 38
Ti-24Nb-4Zr-8Sn [32]	53 ± 1	563 ± 38

under compression and no fracture occurred with strains up to 60%. The Young's modulus and yield strength were compared to results reported in previous works for the TNZT alloy [20, 31] and to a β-Ti-24Nb-4Zr-8Sn alloy produced by L-PBF [32].

A lower Young's modulus is observed for the unidirectional-Y sample, due to the strongest texture along the direction ⟨001⟩, which is the same direction of the compression tests. Therefore, it is shown that the grain alignment in this direction may contribute to the reduction of Young's modulus required for applications such as medical implants [33]. In addition, the samples produced using the unidirectional-Y scanning strategy presented higher porosity, which contributes to a higher standard deviation of the Young's modulus when compared to the CHB and R79 scanning strategies. To clarify this, nanoidentation shall be performed in future works.

The samples produced with the R79 strategy showed the highest yield strength. Based on the microstructural features (Figs. 4 and 5), this result can be associated with a lower porosity observed in the samples with the R79 scanning strategy. The microstructure of samples with the CHB strategy consists of more equiaxed and smaller grains in comparison to the R79 scanning strategies. In addition, the CHB strategy resulted in a more randomly oriented grain structure. Therefore, a more isotropic mechanical response is expected and shall be validated in future works with tensile tests. Nevertheless, samples produced with the CHB strategy presented higher porosity than in the R79 strategy (Figs. 2 and 3), which resulted in a slightly lower yield strength for the CHB strategy.

Finally, it is seen that Young's modulus and compressive strength of the samples produced with the different scanning strategies are similar to the TNZT as-cast [31], proving the feasibility of designing the microstructure of the TNZT alloy by L-PBF developing the scanning strategy.

Conclusions

In this work, three different scanning strategies were used in the L-PBF of the TNZT alloy, while keeping the laser parameters constant. The main findings are:

- The variation of the scanning strategy affected the type and distribution of pores. Lack-of-fusion was observed with pores aligned in the direction of the scanning vector within the layers in the unidirectional-Y scanning strategy, while rotating the vectors in the R79 and CHB scanning strategies resulted in a more homogeneously distributed circular pores. The CHB strategy also resulted in a concentration of pores along the boundaries of the islands.

- The scanning strategy did not show influence on the TNZT alloy phase constitution, and a cellular solidification structure was observed in all cases. Nonetheless, the influence on the heat distribution was observed on the melt pool. Samples with the R79 scanning strategy showed the greatest values for the melt pool depth, while unidirectional-Y and CHB resulted in shallower melt pools due to a constant remelting of previous layers.

- The unidirectional-Y strategy resulted in samples with fiber texture along the $\langle 001 \rangle$ direction. The CHB scanning strategy resulted in a randomly oriented and heterogeneous grain structure with equiaxial grains forming in the contours of the islands and columnar grains in the center. The R79 strategy resulted in a weak tendency of grain alignment along the $\langle 001 \rangle$ direction.

- The R79 scanning strategy resulted in the highest yield strength due to lower porosity. On the other hand, the lowest Young modulus was obtained with the unidirectional-Y strategy sample, due to fiber texture in the <001> direction. The unidirectional-Y strategy also produced the samples with highest porosity, which also contributed to its lower Young's modulus.

Experimental procedure

Material

TNZT (wt%) pre-alloyed powder with particle size between 45 and 106 μm was used for producing the samples by L-PBF. Chemical analysis was carried out by inductively coupled plasma-optical emission spectroscopy (ICP-OES, Varian vista AX CDD). The analysis of oxygen content was obtained with infrared absorption and thermal conductivity (LECO OHN-836).

The powder particles' morphology was analyzed via scanning electron microscopy (SEM, Phillips FEG XL-30) to investigate the sphericity, the presence of *satellites* and pores (Fig. 2). For microstructural analysis, samples were metallographically prepared with a final polishing step of 1.0 μm and etched with a solution of 5 mL HF (40% concentrated) + 10 mL HNO$_3$ (65% concentrated) + 85 mL H$_2$O.

Sample preparation

Cylindrical samples (10 mm in length and 5 mm in diameter) were produced in a Realizer SLM 50 device equipped with a fiber laser in continuous mode ($\lambda = 1070$ nm, focus position F:

9.55 mm, spot size ~ 60 μm) and a baseplate of pure Ti (grade 2). The chamber was purged with argon during all experiments for minimizing the oxygen content of the atmosphere (< 0.1 wt%).

All samples were manufactured using the following parameters: 129 W of laser power, scanning speed of 0.57 mm/s, hatching distance of 110 μm, and layer thickness of 40 μm. These parameters were previously optimized and reported by Batalha et al. [31]. With all parameters fixed, the scanning strategy was varied in three modes: unidirectional in the *y*-axis without rotation [unidirectional-Y, Fig. 6(a)], bidirectional with 79° rotation between layers [R79, Fig. 6(b)], and chessboard bidirectional with 90° rotation between islands of 1.5 mm^2 [CHB, Fig. 6(c)]. The 79° rotation between layers in R79 scanning strategy was selected to delay the laser remelting of same track in next layers.

Relative density and porosity analysis

The density was measured according to the Archimedes method in a Gehaka DSL910 balance. The relative density was calculated by normalizing the measured absolute density values for a fully dense sample of the TNZT alloy produced by suction casting. A confocal microscope Olympus LEXT OLS 4000 was employed to investigate the pore distribution. X-ray micro-computed tomography (μ-XCT) was additionally performed in transversal and longitudinal sections of the samples to determine the pore size distribution. The measurements were carried out in a GE Nanotom˚ M device, with a voltage of 140 kV, a current of 100 μA, and a voxel size of 5 μm. All scans were reconstructed using the VGStudio Max 2.2.7 software, and the analysis was performed with the Avizo 9.4.0 software package.

Microstructure and mechanical characterization

The chemistry of the bulk samples was also analyzed by ICP-OES, infrared absorption, and thermal conductivity. The microstructure of the samples was investigated in the longitudinal section of metallographically prepared specimens, using an optical microscope (OM – Olympus BX41M-LED) and an SEM (Phillips FEG XL-30 and FEI Inspect S50). Chemical microanalysis was performed via energy-dispersive X-ray spectroscopy (EDS, Bruker) coupled to the SEM.

The phase identification of the as-built samples was performed by X-ray diffraction (XRD, Bruker D8 Advanced ECO), with Cu-K$_{\alpha 1}$ radiation at 45 kV and 25 mA in the range 5–90°. The phases were indexed with the software X'Pert HighScore Plus.

Electron back-scattered diffraction (EBSD, Bruker) was used to obtain additional information concerning the microstructure of the samples. The grain size and morphology, and

crystallographic texture were investigated. The analysis was carried out in an FEI Inspect S50 scanning electron microscope, and the EBSD patterns were analyzed in the OIM Analysis software (EDAX). The samples were cut along the longitudinal section and prepared via grinding and polishing with a 1.5 mL HF (40% concentered) + 4 mL (65% concentrated) + 260 mL oxisilicate, followed by polishing in a VibroMet vibratory polisher machine.

The mechanical properties were determined by uniaxial compression testing following the ASTM E9 Standard. The tests were performed in an INSTRON 5500R machine with an initial strain rate of $10^{-4}\,\mathrm{s^{-1}}$. The yield strength was obtained at 0.2% strain ($\sigma_{0.2\%}$). A laser extensometer was used during the compression tests and the Young's modulus of the samples were obtained from the stress–strain curves.

Acknowledgments

Author contributions

WCB: methodology, investigation, writing—first draft. RLB: conceptualization, data curation, formal analysis, investigation, writing—final version. KK: writing—review and editing, visualization, validation. CSK: resources, writing—review and editing, supervision, project administration, funding acquisition. PG: conceptualization, resources, writing—review and editing, supervision, funding acquisition.

Data availability

The datasets generated during and/or analyzed during the current study are available from the corresponding author on reasonable request.

Declarations

Conflict of interest The authors declare that they have no known competing financial interests or personal relationships that could have appeared to influence the work reported in this paper.

Open Access

Supplementary Information

The online version contains supplementary material available at https://doi.org/10.1557/s43578-022-00735-7.

References

1. E. Herderick, in *Materials Science & Technology Conference & Exhibition (MS T'11. 2)* (2011).

2. W.E. Frazier, J. Mater. Eng. Perform (2014). https://doi.org/10.1007/s11665-014-0958-z

3. S.L. Sing, J. An, W.Y. Yeong, F.E. Wiria, J. Orthop. Res. (2015). https://doi.org/10.1002/jor.23075

4. M. Geetha, A.K. Singh, R. Asokamani, A.K. Gogia, Prog. Mater. Sci. (2009). https://doi.org/10.1016/j.pmatsci.2008.06.004

5. B.L. Zhang, H. Attar, Adv. Eng. Mater. (2015). https://doi.org/10.1002/adem.201500419

6. A. Kreitcberg, V. Brailovski, S. Prokoshkin, J. Mater. Proc. Technol. (2018). https://doi.org/10.1016/j.jmatprotec.2017.10.052

7. J.P. Luo, J.F. Sun, Y.J. Huang, J.H. Zhang, Y.D. Zhang, D.P. Zhao, M. Yan, Mater. Sci. Eng. C. (2019). https://doi.org/10.1016/j.msec.2018.11.077

8. Y.J. Liu, X.P. Li, L.C. Zhang, T.B. Sercombe, Mater. Sci. Eng. A (2015). https://doi.org/10.1016/j.msea.2015.06.088

9. E. Bueno, V. Andre, R. Henriques, C. Roberto, C. Alberto, A. Cairo, Mater. Res. (2007). https://doi.org/10.1590/S1516-14392007000300013

10. W. Zhang, A. De, A. Wilson-Heid, A.M. Beese, J.W. Elmer, J.S. Zuback, T. Mukherjee, J.O. Milewski, T. DebRoy, H.L. Wei, Prog. Mater. Sci. (2017). https://doi.org/10.1016/j.pmatsci.2017.10.001

11. C.Y. Yap, C.K. Chua, Z.L. Dong, Z.H. Liu, D.Q. Zhang, L.E. Loh, S.L. Sing, Appl. Phys. Rev. (2015). https://doi.org/10.1063/1.4935926

12. E.Y. Sefene, J. Manuf. Syst. (2022). https://doi.org/10.1016/j.jmsy.2022.04.002

13. I. Yadroitsev, P. Bertrand, I. Smurov, Appl. Surf. Sci. (2007). https://doi.org/10.1016/j.apsusc.2007.08.046

14. J. Song, W. Wu, L. Zhang, B. He, L. Lu, X. Ni, Optik (2018). https://doi.org/10.1016/j.ijleo.2018.05.128

15. E.H. Valente, C. Gundlach, T.L. Christiansen, M.A.J. Somers, Appl. Sci. (2019). https://doi.org/10.3390/app9245554

16. J. Han, A study on the surface quality of the 3D printed parts caused by the scanning strategy. Rapid Protot. J. **25**(2), 247–254 (2019)

17. H. Schwab, F. Palm, U. Kühn, J. Eckert. Mater. Des. (2016). https://doi.org/10.1016/j.matdes.2016.04.103

18. I. Barin, *Thermochemical Data of Pure Substance*, 3rd edn. (Wiley-VCH, Weinheim, 1995)

19. T. Gustmann, A. Neves, U. Kühn, P. Gargarella, C.S. Kiminami, C. Bolfarini, J. Eckert, S. Pauly, Addit. Manuf. (2016). https://doi.org/10.1016/j.addma.2016.04.003

20. R.L. Batalha, V.E. Pinotti, O.O.S. Alnoaimy, W.C. Batalha, T. Gustmann, K. Kosiba, S. Pauly, C. Bolfarini, C.S. Kiminami, P. Gargarella, J. Mater. Res. (2021). https://doi.org/10.1557/s43578-021-00422-z

21. M. Kheradmandfard, S.F. Kashani-bozorg, K. Kang, J. Alloys Compd. (2018). https://doi.org/10.1016/j.jallcom.2017.12.049

22. C.R.M. Afonso, P.L. Ferrandini, A.J. Ramirez, R. Caram, Acta Biomater. (2010). https://doi.org/10.1016/j.actbio.2009.11.010

23. E. Yasa, J. Deckers, J. Kruth, Rapid Prot. J. (2011). https://doi.org/10.1108/13552541111156450

24. Y. Li, Y. Ding, K. Munir, J. Lin, M. Brandt, A. Atrens, Y. Xiao, J. Rakesh, C. Wen, Acta Biomater. (2019). https://doi.org/10.1016/j.actbio.2019.01.051

25. T. Ishimoto, K. Hagihara, K. Hisamoto, S. Sun, T. Nakano, Scr. Mater. (2017). https://doi.org/10.1016/j.scriptamat.2016.12.038

26. L. Zhou, T. Yuan, R. Li, J. Tang, G. Wang, K. Guo, J. Yuan, Powder Technol. (2019). https://doi.org/10.1016/j.powtec.2018.09.073

27. W. Chena, C. Chena, X. Zia, X. Chenga, X. Zhanga, Y.C. Linb, K. Zhoua, Mater. Sci. Eng. A (2018). https://doi.org/10.1016/j.msea.2018.04.087

28. J. Zhao, X. Xue, B. Wang, T. Liu, L. Luo, L. Luo, Y. Wang, L. Wang, Y. Su, J. Guo, H. Fu, Mater. Sci. Eng. A (2021). https://doi.org/10.1016/j.msea.2021.141889

29. G. Jing, Z. Wang, J. of Mater. Proc. Tech. (2021). https://doi.org/10.1016/j.jmatprotec.2021.117188

30. H.L. Wei, J. Mazumder, T. DebRoy, Sci. Rep. (2015). https://doi.org/10.1038/srep16446

31. R.L. Batalha, W.C. Batalha, L. Deng, T. Gustmann, S. Pauly, C.S. Kiminami, P. Gargarella, J. Mater. Res. (2020). https://doi.org/10.1557/jmr.2020.90

32. L.C. Zhang, D. Klemm, J. Eckert, Y.L. Hao, T.B. Sercombe, Scrip. Mater. (2011). https://doi.org/10.1016/j.scriptamat.2011.03.024

33. S.-H. Leea, M. Todaia, M. Taneb, K. Hagiharac, H. Nakajimab, T. Nakanoa, J. Mech. Behav. Biomed Mater. (2012). https://doi.org/10.1016/j.jmbbm.2012.05.005